Optics & Laser Technology 151 (2022) 108027

Contents lists available at ScienceDirect

Optics and Laser Technology

journal homepage: www.elsevier.com/locate/optlastec

Multi-beam optical phase array for long-range LiDAR and free-space data communication

Yunhan Wu [a,b], Shuai Shao [a,*], Yixuan Li [a,b], Xiangzheng Chen [c], Dongbo Che [a,b], Jiayu Chen [a,b], Kunyang Du [a,b], Ruitao Jiang [a,b], Xunqing Huang [a,b], Dongping Kan [d]

[a] State Key Laboratory of Laser Interaction with Matter, Changchun Institute of Optics, Fine Mechanics and Physics, Chinese Academy of Sciences, Changchun 130033, China
[b] University of Chinese Academy of Sciences, Beijing 100049, China
[c] Key Laboratory of Electro-Optical Countermeasures Test & Evaluation Technology
[d] Liaoning Luping Machinery Co., Ltd., Liaoning 112000, China

ARTICLE INFO

Keywords:
Multi-style optical phased array
LiDAR
Free-space optical communication (FSO)
Multi-beam steering

ABSTRACT

We present a multi-beam optical fiber phased array (OPA) with simultaneous light detection and ranging (LiDAR) and free-space optical communication (FSO) data transmission functions. The OPA component can achieve a stable phase and a high turning speed. First, the 55-element OPA is phase-locked through the stochastic parallel gradient descent (SPGD) algorithm to maintain the high light intensity of the main beam in real time. The OPA with a 5 × 11 beam array achieved a wide field of view (FOV) of 58° × 32°, a single beam array steering angle of0.48°, and a steering speed of 40 MHz. Subsequently, this OPA was used to detect targets within a range of approximately 2 km, and we theoretically verified that two-dimensional coherent frequency-modulated continuous wave (FMCW) LiDAR could extract the target characteristics. In addition, a free-space optical communication link of up to 3 km was also demonstrated, with a data rate of 8 Gbps. The proposed system easily increases the array-to-MHz steering speed and yields a high-power output.

1. Introduction

Beam control is a key technology for light detection and ranging (LiDAR) system, and has attracted widespread attention in autonomous vehicles [1], robotics [2], atmospheric measurements [3] and sensing [4]. Many beam steering technologies have been proposed, such as purely mechanical scanning, microelectromechanical systems (MEMS) [5,6], liquid crystals [7], and optical phased arrays (OPAs) [8]. OPAs are an effective approach to beam control; and have become a research hotspot. Mechanical beam steering devices are no longer suitable for meeting the increasing requirements of a more compact low cost and high-resolution LiDAR system, because of the moving parts and complicated calibration. OPA is not limited by the physical and mechanical wear of the inertial components; and facilitates a fast-scanning field of view (FOV) and random scanning of several points. By modulating the light phase and wavelength of the transmitting antenna in the array, the combined beam can be controlled in the far field [9]. The OPA can integrate lasers and other optical elements on a single chip. Large-scale integrated silicon photonic phased arrays were demonstrated by Sun et al. [10] in 2014, including two passive-phased arrays (64 × 64 and 32 × 32) with the ability to generate complex holographic images, demonstrating tremendous progress with respect to scale, performance, and system integration. There are many types of integrated OPAs [11], such as photonic integrated circuits [12]; and commercial CMOS processes with monolithic electronics and photonics [13,14]. However, because of the limitation of the processing technology; and the irreducible distance between the adjacent transmitting unit antennas of an OPA, an OPA typically has a narrow scanning range and lacks a wide FOV [15]. Y.Q. Liu proposed that scanning multiple beams can reduce the scanning angle; and ensure a wide FOV with a large-element spacing OPA. Recently, a beam control technology based on on-chip switch/antenna structures and on-chip lenses has received widespread attention. In this case, the beam steering is achieved using an integrated switch to switch between the transmitters, and the lens is used to control the beam steering [16,17].

Rapid and precise beam steering is crucial in free-space optical applications that require random-access pointing and agile stabilization. The typical OPA-based method for transmitting light beams through a

* Corresponding author.
E-mail address: sshuaiciomp2021@163.com (S. Shao).

https://doi.org/10.1016/j.optlastec.2022.108027
Received 30 August 2021; Received in revised form 24 February 2022; Accepted 28 February 2022
Available online 15 March 2022

liquid crystal (LC) phase shifter array was demonstrated by McManamon in 2009 [18]. One-dimensional (1D) OPAs; with unequal spacing utilizing phase tuning have been used for large-angle steering. High-speed and high-power beam control have been demonstrated using a six - element 1D OPA with unequal spacing, along with phase-locked beam control modes and scan periods [19,20]. However, there has been no further study and application of 2D OPAs for this architecture.

The rise of mature OPA processing technology has facilitated direct applications, including LiDAR, free-space optical communication (FSO); [21–23] and image projection [24,25]. Coherent solid-state LiDAR using OPA has achieved simultaneous distance and velocity measurements with a 2 m range and a resolution of 20 mm [26]. Because the OPA-based LiDAR has obvious advantages over the other methods in term of low cost, small size, and high resolution, it has attracted significant interest. Highly integrated and miniaturized launch modules are suitable for various scenarios. The OPAs are considered as useful devices for steering a laser beam that can load high-speed data. A transmission rate of 12.5 Gbps has been reported with a 1 × 4 OPA at a distance of 1.4 m [27]. These studies demonstrate the potential of data transmission using the OPAs. However, these chip-scale OPAs are not suitable for high-power beamforming applications, and the detection and communication distances are limited by atmospheric factors. Thus, these chip-scale OPAs exhibit, detection and communication abilities only for indoor applications or at nearer distances.

In this study, we demonstrated a coherent LiDAR and FSO based on a fiber OPA. The OPA used high-bandwidth DC-coupled electro-optic phase modulators (EOMs) to control the phase of each element individually in the array; The fiber array transmitter used a silicon V-groove and a silicon cover to couple the fiber, and a microlens array with a divergence angle of 13.9 mrad was employed. Subsequently, by combining these components, the OPA layout was optimized, and a non-uniformly arranged multi-beam emission 2-D OPA with 5 × 11 elements was proposed. This OPAs was capable of a high-power operation (maximum output power of 24 W), exhibited a wide FOV (58° × 32°), enabled high-speed beam steering (~40 MHz); and exhibited phase lock accuracy (λ/25) with a narrow beam-array steering angle of 0.95°. Taking advantage of the high-power output, we used this OPA to demonstrate a LiDAR system with a 3 km detection range in the outdoors. It was verified that it represents a coherent frequency-modulated continuous-wave (FMCW) LiDAR system capable of synchronous distance and speed measurements. Based on this, we developed an optical wireless transmission system using an OPA; and demonstrated a high-speed data transmission speed of up to 8 Gbps at a distance of 3 km by selecting suitable components for the transmitter and receiver.

2. Operating mechanism and design rules

In the design, a high-precision long-line dense optical fiber array was used to locate the fiber's end face. The transverse and vertical offset errors of the end face of the optical fiber can be limited by the structure of the silicon V-groove bottom plate-fiber-silicon cover plate. Simultaneously, the axial deviation of the fiber in the array must be limited. For the input-end array, the axial deviation changes the normal line of the fiber end face, increases the incident angle of the normally incident light and normal line of the fiber end face, and produces light-reflection loss at the incident surface. A silicon V-groove bottom plate with a thickness of 500 μm and a silicon cover plate with a thickness of 100 μm were used. The design scheme is illustrated in Fig. 1(a). The sidewalls of the optical fiber and the adjacent optical fiber jointly limit certain characteristics. The opening width of the designed V-shaped groove is larger than the diameter of the optical fiber, and the silicon cover is designed as a trapezoidal groove, which can avoid trapezoidal grooves on the silicon base plate and the cover plate to the maximum extent. There are slight deviations in the structures. An optical fiber with a diameter of 127 μm

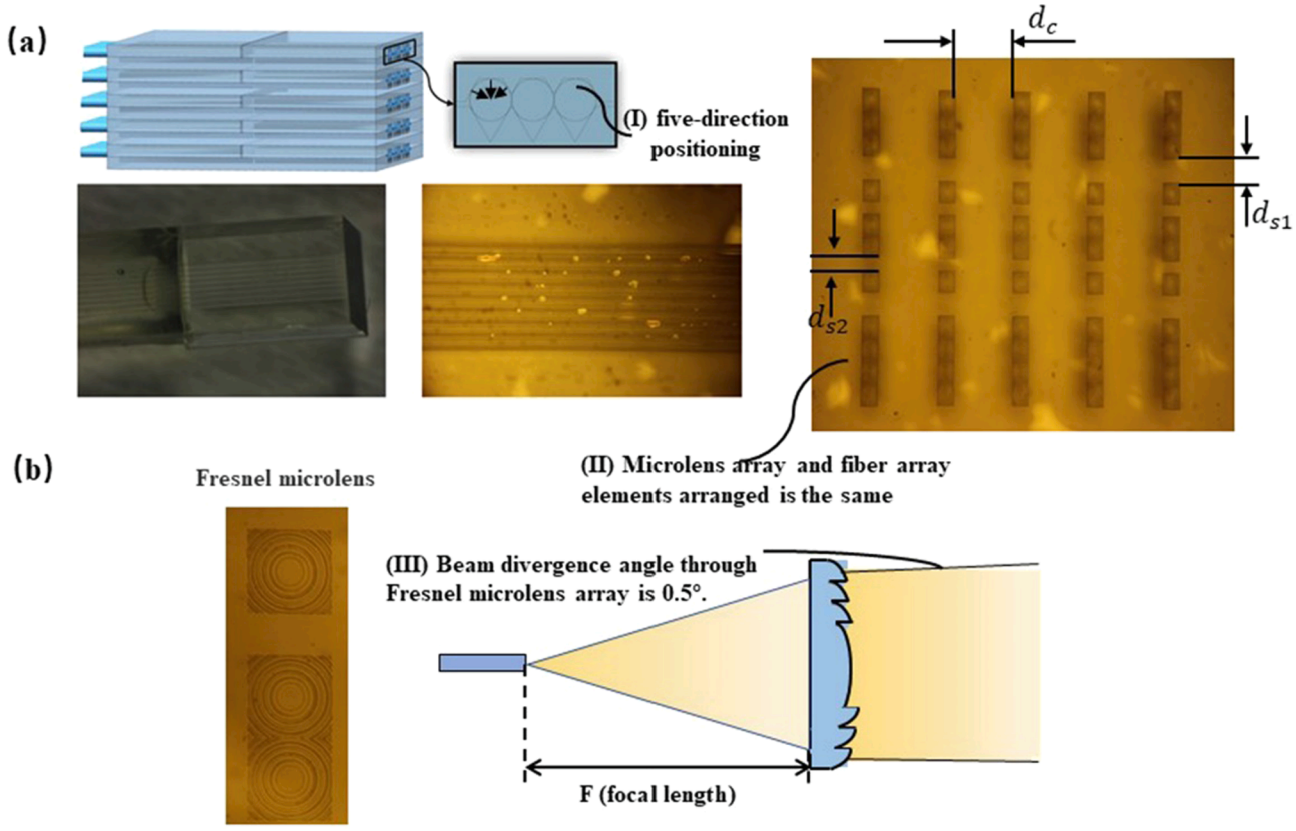

Fig. 1. Schematics of the fiber array and microlens. (a) structure diagram and SEM image of the 55-channel fiber array. (b) Collimation of the beam by the Fresnel microlens array.

(prepared by removing the coating layer of the optical fiber in the 144-core optical cable) is restrained and positioned by the silicon base plate, silicon cover plate, and glass cover plate. The optical fibers are densely arranged in parallel in the V-shaped groove of the silicon base plate. The optical fiber array; and silicon cover plate forms a five-direction positioning optical fiber at the front end of the silicon base plate and the V-shaped groove of the silicon base plate; the glass cover plate is cut from a flat glass with a flatness of <0.2 μm/cm^2; and is placed on the silicon base plate. The back end of the optical fiber was pressed tightly, and a glue container is placed between the silicon cover and the glass cover. The press the glass cover plate is pressed to ensure that the back of the optical fiber is close to the bottom of the V-shaped groove of the silicon bottom plate, and then the silicon cover plate is pressed to bring the front end of the fiber close to the two sides of the V-shaped groove. Then the silicon cover plate was used to press the optical fiber twice, completing the positioning of the optical fiber. A 2D optical fiber array was formed by stacking 1D linear optical fibers in a closed row. Because of the limitations of the current processing technology, the columnar spacing is 550 μm. A microlens array at the output-end surface of the fiber array was used to increase the fill factor of the array; for collimation, as illustrated in Fig. 1(b), the divergence angle of the emitted beam is0.5°, and the fill factor is up to 90 %.

Fig. 2 shows a schematic layout of the proposed multi-beam steering OPA. Light from a 3 W, 1064 nm fiber laser (narrow-linewidth 8 MHz) is split into 55 channels, which are guided through the EOMs, that apply the pseudorandom binary sequence (PRBS) codes, beam steering signal, and phase synchronization feedback to each element. Each channel has an individually controlled phase shifter. Compared to multiple components sharing a phase shifter to realize the phase difference through a delay line connection, parts of the transmitted wavefront cannot be controlled independently. The phase control of a separate component increases the control complexity, and the transmitted wavefront has a greater flexibility. In this study, a commercial phase modulator (1064 nm $LiNbO_3$, maximum input power of 100 mW) was used to reduce the difficulty of component manufacturing. Switching was achieved by applying a voltage to the phase modulator and changing the waveguide refractive index based on the electro-optic effect. The measured phase shift versus electrical voltage is shown in Fig. 3(a). The phase modulator supports a full range of phase shift of 2π, the bias voltage ranges from 0.1 V to 2.1 V, and the half-wave voltage (Vπ) is 2.1 V. The phase modulator exhibits a measured insertion loss of 5 dB and power consumption of 16 mW at a 2π phase shift.

The 55 output elements are connected to the phase shifter form a 5 × 11 2D array. The near-field pattern is shown in Fig. 3(b), in which 55 equally bright light spots were observed. The fiber in the x-direction is observed non-uniformly and sparsely placed. The arrangement (spacing 1:1:2:1.5) is shown in Fig. 1. The fiber array has an equal spacing of 0.25 mm in the y-direction. The alignment and packaging of the microlens array and the optical fiber array are shown in Fig. 3(c). The focal plane overlaps with the surface of the fiber array.

For the OPA presented here; a high-bandwidth DC-coupled EOM was used to control the phase of each element individually in the array, achieving wavefront and megahertz bandwidth beam control. A pinhole was used to employ a silicon photodetector (Thorlabs PDA100) to sample the far-field intensity on the axis and send the electrical signal to the field-programmable gate array (FPGA) control board. The active phase control system of the FPGA development board uses the Black Gold Xilinx Artix-7 development board with an XC7A35T-2FGG484I core chip. The high-speed AD chip used by the A/D sampling module was AD9238, with two conversion channels, a sampling frequency of 65 M, and a sampling number of 12 bits. The D/A module adopts AD9767 chip with a; sampling frequency of 125 M; and an output voltage range of −5 V to + 5 V. The device is used for phase sensing and feedback control signals to stabilize the relative phase of the transmitting unit. It uses a PRBS encoded on each transmitting unit to measure its relative phase; and uses a 1 kHz jitter frequency to determine the amount of phase correction required to maximize the on-axis intensity. This technology has been demonstrated using a high-power OPA [19]. Fig. 4(a) shows the coaxial intensity trajectory of SPGD closed loop and open loop, and its enlarged view shows a convergence time of approximately 100 ms. Because of the thermal noise in the optical fiber and the opto-mechanical phase shift significantly reduces caused by external conditions, the time required for the controller to execute the open loop needs to be limited. If the open loop time is too long, then the phase shift significantly reduces the on-axis strength. We call this the phase loss of the lock. The phase needs to be re-locked, and beam steering control is not performed at this stage. After the second phase-lock cycle, the open loop is turned on again to implement steering control. We call this stage the open loop-phase lock-open loop-lose lock-relock-scan. Fig. 4(b) illustrates the toggling operation.

Here, it is necessary to reasonably control the turn-on period of the phase controller for steering to avoid crosstalk with the phase lock. During the phase-lock cycle, the phase modulators used for steering are turned off, to ensure that they do not interfere with the active feedback.

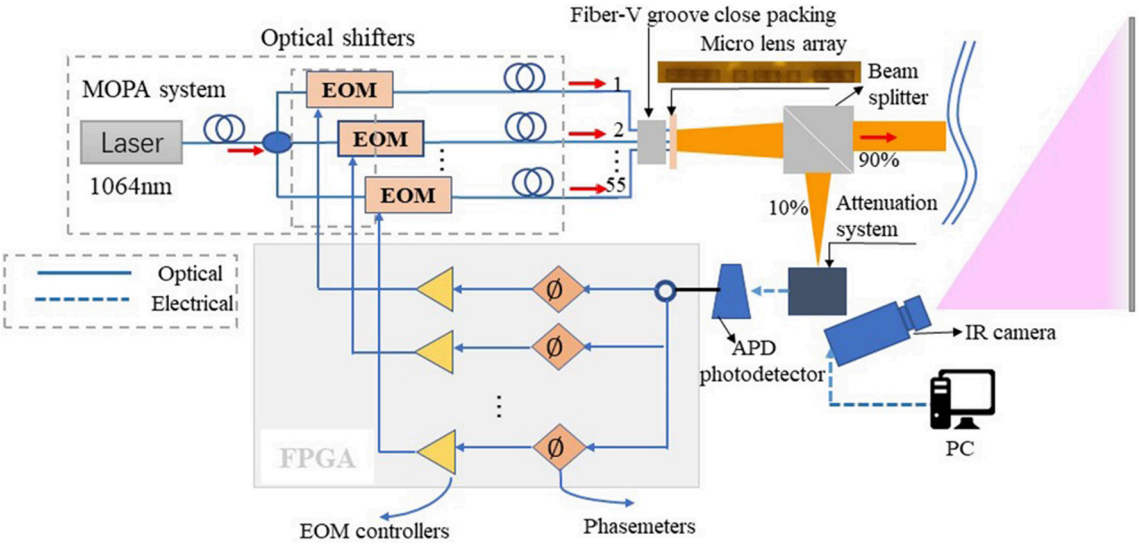

Fig. 2. Schematic layout of the proposed multi-beam steering OPA. FPGA, field-programmable gate array; ADC, analog-to-digital converter; DAC, digital-to-analog converter; EOM, electro-optic phase modulator.

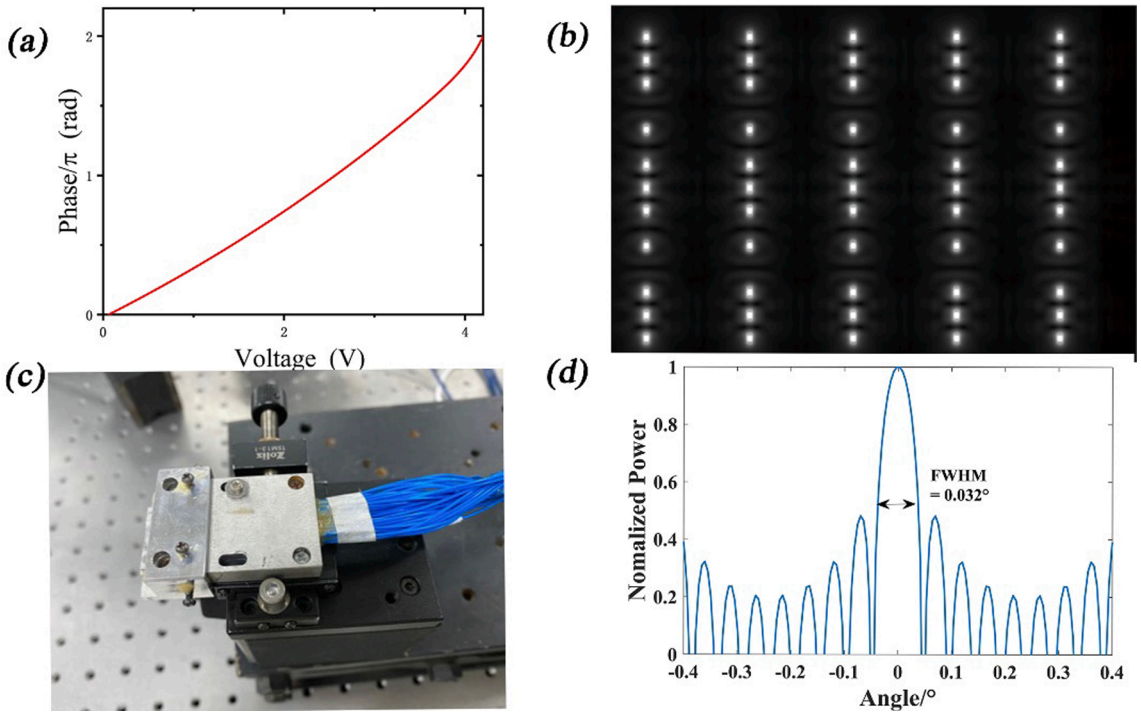

Fig. 3. (a) Measured phase shift versus electrical voltage. (b) Output spots for illustration purpose. (c) Packaged fiber array and microlens. (d) Magnified view of the main beam at 0° with a beam size of 0.032° (FMCW).

In the active phase-locked loop, the SPGD algorithm based on bilateral disturbance corrects the phase of each unit element, and generates a set of small random disturbance signals that obey the Bernoulli distribution to control the bias voltage. During the steering cycle, the feedback voltage switch of the SPGD controller is closed, the SPGD controller bias currents are maintained at the last values of the phase-lock cycle, and the phase modulators are turned on. The digital square-wave signal is sent to the SPGD controller, and the modulation signal of the phase modulator is sent to the phase-shifter control port. The phase-modulator voltage is regulated by the SPGD controller. The phases of the phase locking-scanning-scanning-phase locking-phase locking-scanning-phase locking and scanning periods, as shown in Fig. 4(c). The duration of the phase-locking cycle and the convergence time of the SPGD can be seen in the scanning-phase locking process illustrated in Fig. 4(c_2), where the time of the phase-locking cycle must not be shorter than the convergence time of the SPGD (~100 ms). We set the phase-locking period duration to 200 ms, twice the convergence time (100 ms) to ensure convergence.

3. Integrated beam steering

The experimental setup is shown schematically in Fig. 2. This OPA contain 55- element and has an aperture area of ~ 3.68 mm^2. The integrated design of the chip and the microlens array is directly matched in one molding, thus reducing the energy loss of the main lobe caused by the tilt of the optical axis in the system, and improving the energy concentration of the main lobe of the beam by improving the system assembly and adjustment errors. The phase distribution of the elements was calibrated (phase-lock cycle) and a look-up-table was generated for beam steering. Because of the difficulty of manufacturing the optical fiber array, the distance between the array elements is much larger than half of the free space wavelength ($\lambda/2$, no grating lobes), reducing the crosstalk. The genetic algorithms (GA) are used to optimize the arrangement. Using the sparse and aperiodic nature of the emitters covering a large aperture, we used 55 elements to achieve a large FOV. In contrast, the traditional periodic λ-pitch design requires comparatively more number of elements to achieve the same FOV and FWHM beam width. Utilizing sparsity and aperiodicity, we achieved a low-divergence beam over a wide FOV, relaxing fabrication constraints and optical crosstalk at shorter wavelengths. Fig. 3(c) shows a magnified view of the main beam at 0°, with an FWHM beam width of0.032°. Compared to the evenly spaced array, the non-equal-spaced array element distribution exhibits a 12-dB side lobe suppression, which indicates that optimizing the array element distribution can increase the amplitude of the main beam. Fig. 5(a) shows the 1D calculation results. The elements in the x-direction can emit a 1 × 11 multi-beam arrays, which can be scanned along the deflection angle of a single beam, with the angle range of 74.7°. Fig. 5(b) shows the 2D radiation pattern of the 1D multi-beam transmission OPA.

Considering the limitations of modern packaging technology and the assembly process of the microlens array, the left and right array elements are susceptible to pressure from the packaging fixtures, such that the optical axis changes; and the horizontal and vertical spacing of the array are also different. By combining the structures described above, a 2D multi-beam OPA was demonstrated. Fig. 6(a) shows the 2D radiation pattern of the multi-beam-emitting OPA, exhibiting a clear 4 × 11 spot pattern. The angular separation between the main beam and the first-order beam in the vertical direction was0.1°. By applying various voltages to the SPGD controller, a variety of optical phase configurations can be achieved in the 4 × 11 phase array, and various radiation patterns can be dynamically generated in the far field, as shown in Fig. 6(b). The focused beam spot can be shifted by π rad in each unit cell, and the entire beam array is shifted by approximately 0.5° along the x-direction. Fig. 6 (c) shows that the total FOV of the OPA, indicated by the red dash box, is58° × 32°, which is consistent with that obtained theoretically. The separate phase control module used in this architecture can also realize various light phase configurations in the y-direction, and the beam is deflected in the y-direction. The large number of elements and large apertures of the OPA facilitate high-resolution scan patterns. Independent phase control improves the scanning rate of a 2D beam. In addition, the selective endowment of the phase of the phased array can achieve a completely random scanning pattern, and it has the capability of expansion for the scale of the phased array. This not only increases the

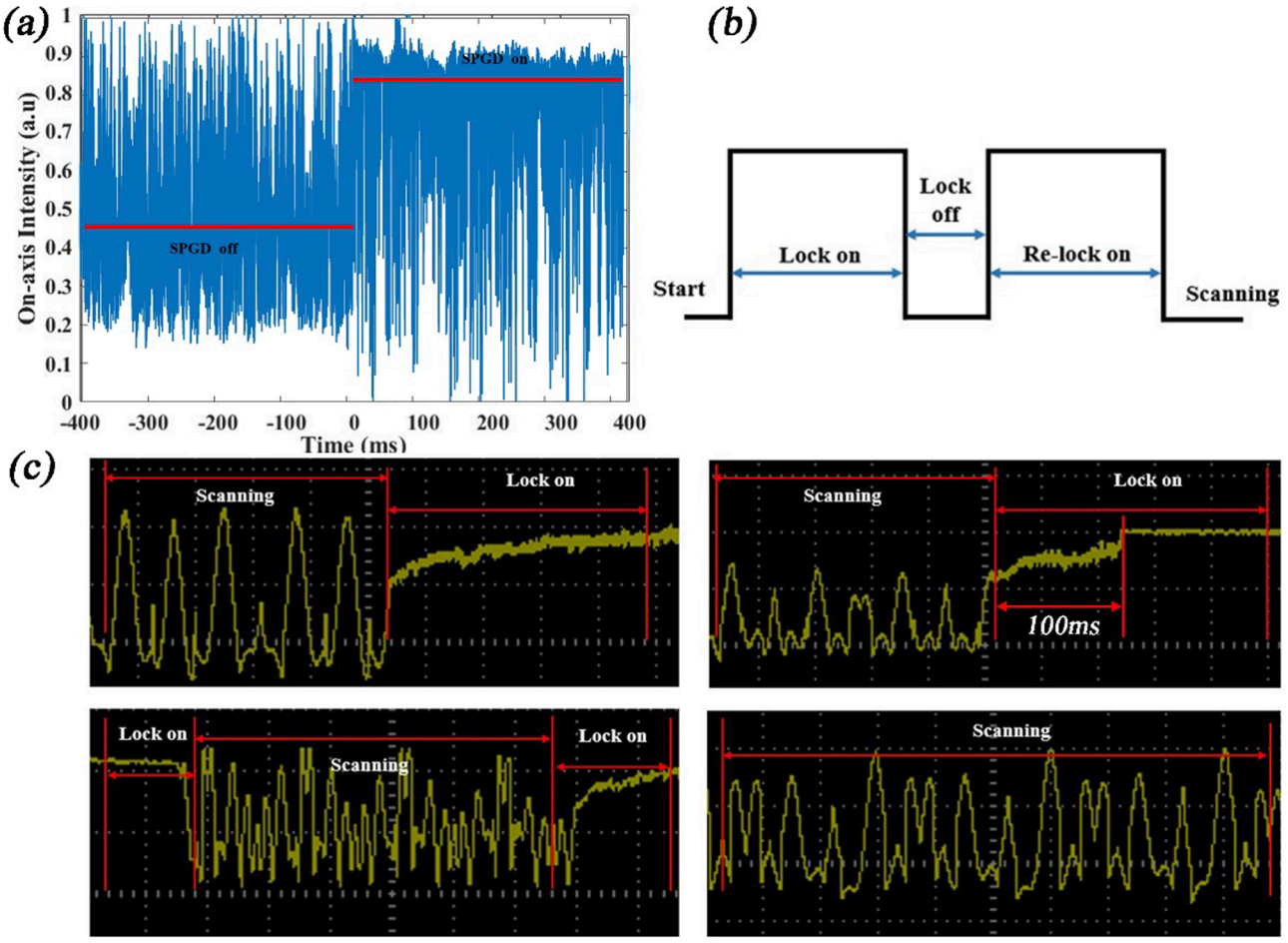

Fig. 4. (a) Phase-lock convergence trace. (b) Illustration of toggling modality. (c) Both phase locking and scanning modes, (c_1) phase locking and scanning periods, (c_2) scanning and phase locking periods, (c_3) phase locking and scanning and phase locking periods, and (c_4) scanning periods.

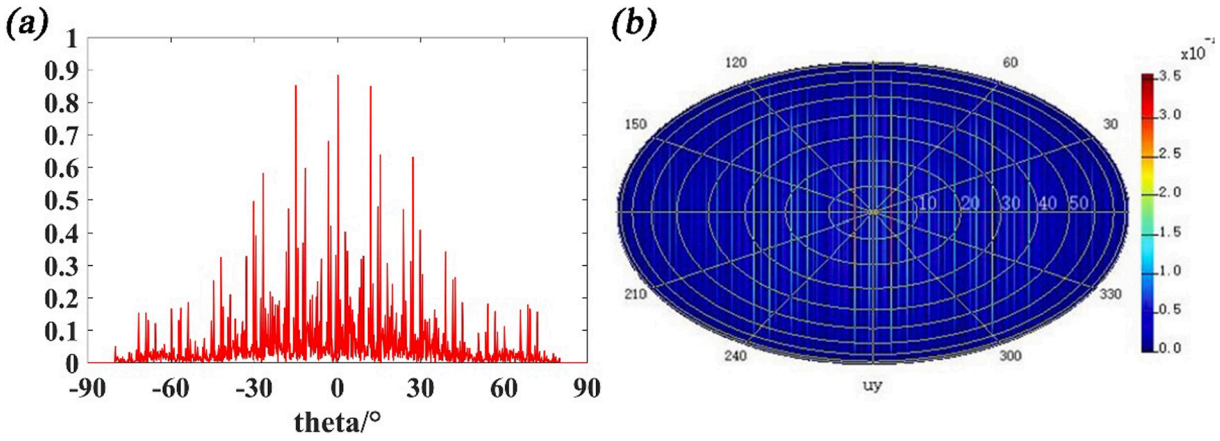

Fig. 5. Calculation results for the 1D multi-beam-emitting OPA. (a) Far-field pattern of the unequal spacing OPA. (b) 2D radiation pattern of the OPA.

LiDAR's FOV; but also increases the point density of a certain position in the FOV.

Notably, the distance between the transmitting units of the proposed OPA is larger than that of a typical OPA with a large steering. Moreover, the proposed phased array also has the advantages of array expansion and high-power beamforming. As the degree of design freedom increases, a smaller pitch size may help improving the scanning efficiency and uniformity of the beam array. However, it is difficult to achieve acceptable device performance using designs based on the traditional manufacturing techniques. We can consider arranging the fiber core (10 μm) for coupling, taking into account factors such as high-power transmission, and optimizing the array element spacing and the size of the core.

4. LiDAR with integrated optical phased array

The OPAs described above provide a feasible solution for LiDAR applications through stable control and flexible beam steering

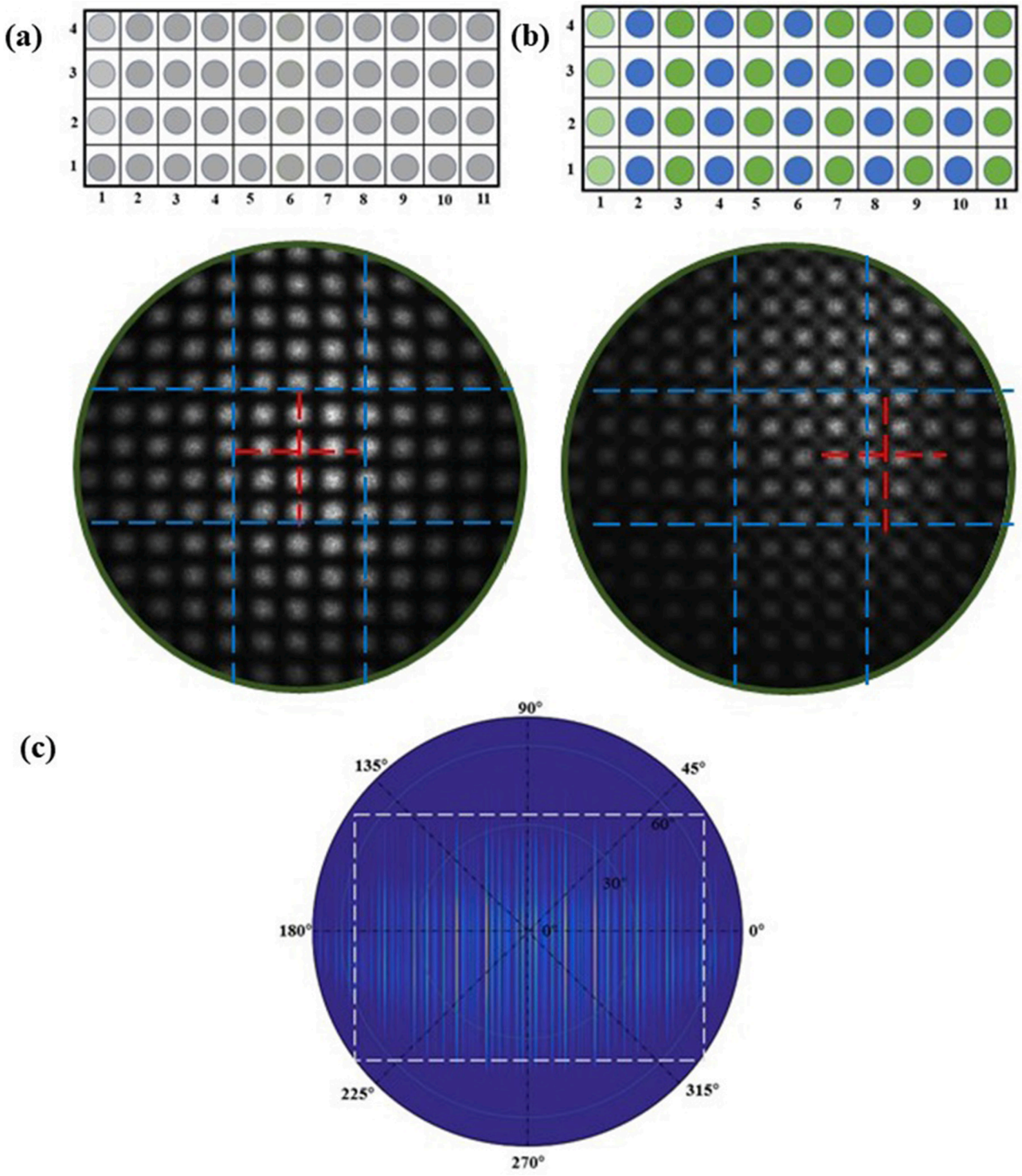

Fig. 6. Measurement results of non-uniform 4 × 11 active optical phased arrays. (a) 2D radiation pattern of the OPA with a phase difference of zero. (b) 2D radiation pattern of the OPA with a phase difference of π. (c) Far-field pattern of the OPA; the white dashed box indicates the total FOV.

capabilities. Here, we propose a coherent LiDAR system based on an FMCW OPA chirp, which combines the optical heterodyne and chirp technology. Compared to the traditional pulse time-of-flight technology, this method uses the heterodyne technology to obtain the Doppler frequency shift of the target echo light directly, along with obtain the target motion status. In addition the intensity (surface emission), time correlation, and the radial velocity parameter can also be obtained with high precision. Moreover, the preparation process of the fiber laser phased array is mature and can be highly integrated, and the continuous wave-operation allows the use of efficient and reliable commercial off-the-shelf fiber optic telecommunication components. Transmitting and receiving are performed by the OPA, and ranging within a certain angle range can be easily realized by 1D beam steering. To determine the specific target type, additional target parameters; such as the solid angle; radial velocity; are required. Thus, we consider 3D LiDAR using 2D beam scanning.

As shown in Fig. 7, the OPA coherent LiDAR system primarily uses commercial off-the-shelf equipment, in which the detector is a low-noise

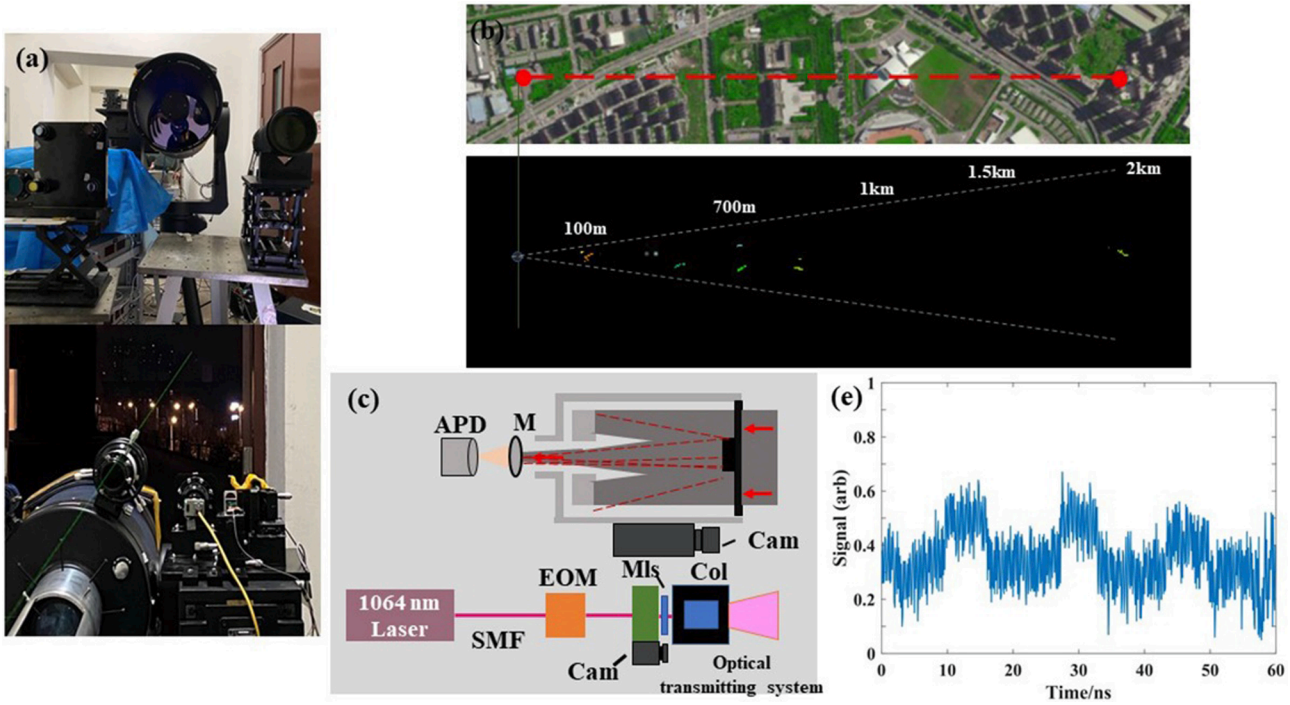

Fig. 7. Illustration of the FMCW LiDAR system over 2 km. (a) Photograph of the setup hardware, including the Transmitting optical system and receiving optical system. (c) Schematic diagram of the experimental setup: Cam, camera; M, mirror; APD, avalanche photodiode; EOM, electro-optic modulator and SMF, single mode fiber. (e) Target return signal waveform received by the detector.

InGaAs APD (avalanche photodiode). The transceiver system includes a Cassegrain telescope with a moderate aperture of 350 mm, which was integrated and fixed on a pitch-rotating platform. For the light source, we used a standard fiber laser (8 MHz, 1064 nm), emitted from a 2D fiber array into free space, and the maximum emission power can reached 40 W. All the optical fibers were polarization-maintaining single-mode optical fibers. Part of the modulated signal light leaving the laser was used as the local oscillator (LO) of the optical receiver, and the other part passed through the high-power fiber laser amplifier and entered the free space through the fiber array. The beam was expanded and collimated by the 38 mm aperture telescope. The acquired target echo light was collected by the receiving telescope and coupled to the optical fiber. A polarization-maintaining fiber combiner was used to mix the received signal light with the LO signal light. The digital oscilloscope connected to it collected and stored the data through an InGaAs APD with a bandwidth of 50 MHz.

Here, we demonstrate that the FWCM LiDAR system outdoors at large distances using direct detection techniques, and echo detection was tested at night to induce interference from the background radiation from stray light, as shown in Fig. 7(a) and (b). If coherent testing technology is used, then the system does not interfere with the ambient light (sunlight) or other background light. Fig. 7(b) shows a real-time data visualization image of the received echo signal used to display the results of the DSP and image processing on the FPGA. The building targets scanned at 300 m, 700 m, 770 m and 2 km can be clearly observed. Fig. 7(e) shows the target return signal waveform received by the detector. Because of the limitations of the test site, only 2 km detection was performed. The same multi-style laser coherent detection test sample parameters were used, including the emission power and laser divergence angle of the laser emission sub-array, laser receiving optical system, laser detector, set detection sensitivity and other parameters, as well as the same measured target and target parameters, and the detectable distance was calculated according to the atmospheric environment parameters at three different detection distances. This technique has previously been demonstrated with an OPA architecture capable of handling power in the order of a few hundred watts, and reaching detection distances in the tens of kilometers.

Coherent LiDAR can; not only directly detect LiDAR signals, as described above, and can acquire various types of information such as position, direction and intensity (target reflectivity), but it can also directly acquire target information such as speed. Therefore, FMCW LiDAR systems have been developed to achieve an acceptable range accuracy and a fine range resolution. The Doppler frequency shift of the target echo light is obtained using the heterodyne method; to collect basic information about the target is obtained. The triangular wave linear frequency modulation (FM) continuous wave radar uses the beat frequency to detect fixed targets, which has unique advantages. Triangular wave linear FM continuous wave (CW) signal is illustrated in Fig. 8 (a); here, A local oscillator (LO),f_t, a frequency-modulated optical received signal (RX), f_r, which follows the same pattern of variation as that of the frequency of emission, but with a time delay, $\Delta t = 2R/c$. The beat frequency between the transmitting and receiving signals is; $f_b = f_t - f_r$. For a stationary target, the Doppler effect need not be considered; thus, $f_b = \frac{2B}{T}\Delta t = \frac{4B}{T \cdot c}R$, where B is the bandwidth of the FM signal, T is the period of the triangular wave FM signal, R is the distance to the target and c is the speed of light. For a moving target, the relative radial velocity of the target is v, considering the effect of Doppler frequency, $f_d = f_0\frac{2v}{c}$, where f_0 is the frequency of the input light. For a triangular wave linear FM continuous wave radar signal within a sweep period T_m, the upper sideband f_{up}, down side band f_{down}, where $f_d = \frac{(f_{down} - f_{up})}{2}$, the target radial velocity, $v = \frac{c(f_{down} - f_{up})}{4f_0}$. By detecting both the sweep frequencies, simultaneous distance and velocity measurements were can be performed.

FWCM LiDAR system with simplified heterodyne detection using a TX OPA is illustrated in Fig. 8(b). This detection configuration is capable of simultaneously detecting the target distance and target velocity. Fig. 8 (c) shows the beat frequency of a stationary target at a distance of 700 m, as$f_b = 148kHz$, and moving target with velocity $v = 10m/s$ at distance of 700 m, where the output spectrum of the detected signal shows that the upper sideband frequency is $f_b = 163kHz$ and downside band frequency

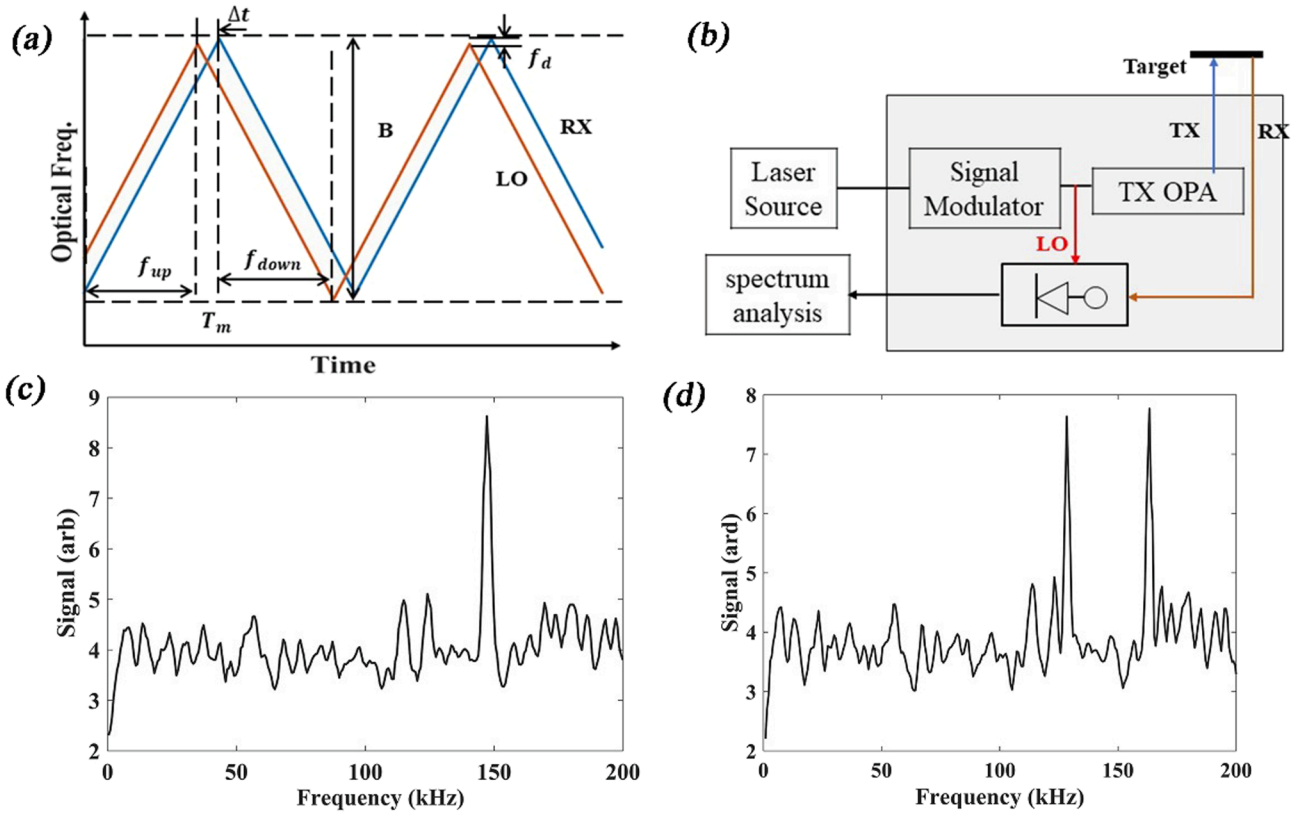

Fig. 8. (a) Concept of FMCW LiDAR with triangular-wave modulation, (b) Schematic of the LiDAR system with transmitting and receiving optical phased arrays, (c) Stationary target at $R = 700\ m$, and (d) Moving target at $R = 700\ m$.

is $f_b = 130kHz$(is shown in Fig. 8(d)). Utilizing the experimental installation shown in Fig. 7, an FWCM LiDAR system was created. Compared to active detection, the laser coherent detection has stringent requirements of wavefront matching conditions of signal light and local vibration light, such as spatially aligned polarization of the same. For the background stray light, the incident direction is chaotic and the polarization state is unstable; thus, it does not form an effective detection signal with a strong spatial filtering capability.

5. Optical free-space data communication

As a result of the continuous development of communication data and the Internet of Things, as well as the current limitations of RF radiofrequency-based communication, free-space optical communication has attracted considerable interest. Moreover, this interest in free-space optical communication has also been fueled by the increase increasing emission power of lasers and sensitivity of photodetectors, as well as by the advancements in the light-wave narrowband filtering technology and light source frequency stabilization technology. The practicality of the technology provides a technical guarantee. Considering the key technologies of the free-space laser communication technology at this stage, under a certain laser emission power, the power distribution within the communication distance is severely restrict; by the atmospheric transmission characteristics of the laser. Second, the FSO system is affected by the atmosphere, and atmospheric attenuation and turbulence shorten the communication distance, reduce the effectiveness, and increase the bit error rate. Finally, the narrow laser beam increases the difficulty of alignment at both ends of the FSO system. Standard components, such as silicon photonics, are tightly integrated, and thus; an OPA with a beam steering function has become the main choice for PSO link transmitters. However, the power of the integrated OPA output laser beam is generally on the milliwatt, or watt level, and the effective PSO communication distance is 50 m −100 m [11], such that atmospheric attenuation and turbulence affect the bit error rate.

Fig. 9(a) shows the experimental setup used to demonstrate the 8-Gbps wireless data transmission performance of the OPA, based on the architecture proposed in Fig. 2. A 1063 nm laser was used to generate an 8-Gbps on–off keying (OOK) signal modulated by a Mach-Zehnder modulator (MZM) driven by PRBS. The modulated optical signal was amplified with an erbium-doped fiber amplifier (EDFA), to attain sufficient optical power, and coupled to a transmitter OPA. The alignment of the transmitter OPA and the receiver is regulated by a coaxial camera; for a total propagation length of 3 km to the receiver (Fig. 9(b)). Four fiber collimators with apertures were placed 3 km away from the transmitter to collect the diverged beam from the OPA. The received beam was sent to an InGaAs APD through a fiber, and the electrical output was analyzed using a sampling scope.

Here, passive OPAs are used to demonstrate a static point-to-point free-space communication link. For the 3 km high-speed long-distance communication link with OPAs, a clean eye of 8-Gbps is observed when the APD is used as the receiver, as shown in Fig. 9(d). The results of this experiment, where packets of data are set from the TX OPA to the APD, are shown in Fig. 9(c), presenting a magnified image of a single block of data. In a subsequent study, we can consider replacing this with an active OPA (described in Section 3) to demonstrate point-to-multipoint configuration. The transmitting OPA exhibiting active phase control is scanned for multiple points, thereby enabling the multiple receivers to receive the signal. In long-distance free-space optical communication, the active OPA can ensure the rapid and high probability acquisition of the communication receiver to ensure the alignment of the communication transmitter axis and the communication receiver axis and establish a communication link. Because of the environmental instability of the optical abutment, the communication light arriving at the receiver side produces a position lag, which needs to be compensated in advance to ensure that the center of the communication beam near the diffraction limit angle is precisely aligned to the receiver side, This is

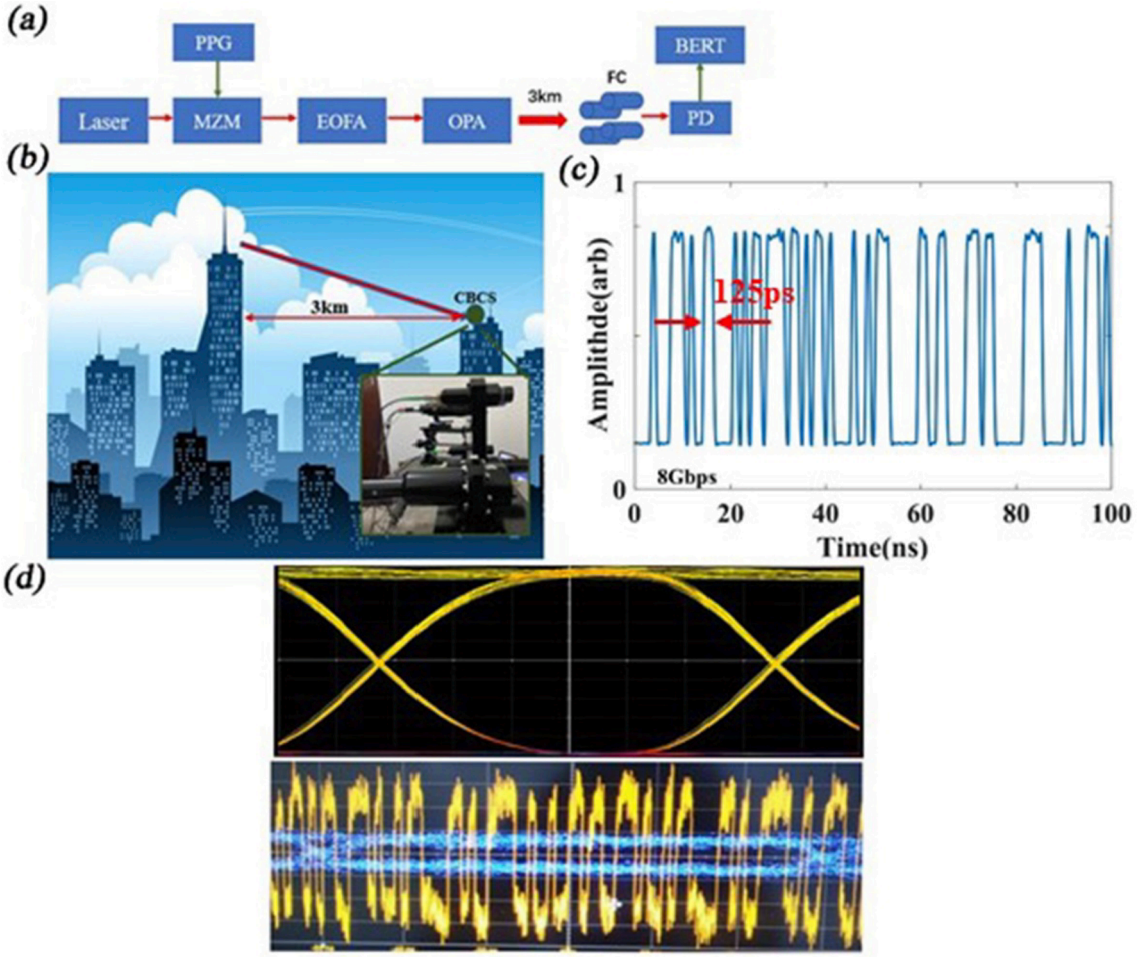

Fig. 9. (a) Experimental setup used to demonstrate the 8-Gbps wireless data transmission performance of the OPA. (PPG: pseudorandom pattern generator; MZM: Mach-Zehnder modulator; EDFA: erbium-doped fiber amplifier; OPA: optical phased array; FC: fiber collimator; PD: photodiode; BERT: BER tester). (b) 3 km optical path from transmitting OPA to receiver. (c) Zoom in of the received data sequence. Received eye diagram (d) at 8 Gbps using an APD receiver.

required to; reducing the power drop caused by the error and satisfy the dynamic communication requirements.

Fig. 10 shows a comparison of the BER data versus receiver power, through the free-space, as explained in the experimental setup in Fig. 9 (a). The power received from the OPA was varied from −18.64 to −19.65 dBm using the EDFA and fiber. The results show that appropriately increasing the output power can effectively reduce the bit error rate. From the perspective of reducing the loss of free space, compressing the divergence angle of the communication beam is one of the main technical approaches. To increase the power density of the receiving terminal as much as possible, so that the area with the largest communication optical power density covers the optical receiver, and enhance the power concentration of the far-field beam, phase-locked modulation can be effectively used.

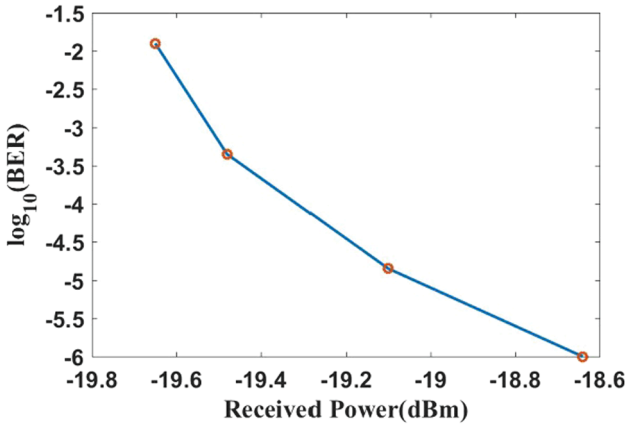

Fig. 10. BER performances of 3 km free-space data transmission through the OPA.

6. Conclusion

We present a multi-beam steering OPA with applications in LiDAR and free-space data communication. In a detailed design process, phase control techniques were combined achieve fast steering (40 MHz) using an OPA, with 55-elements and an efficiency high-power output, covering a total scanning FOV of58° × 32°, and a narrow scanning range of0.5°. Phase synchronization was realized using the SPGD phase-locking algorithm. The non-periodic arrangement of optical phased array and the phase-locked control technology of each beam can improve the beam scanning performance. A 2D LiDAR system with OPAs was used to detect diffuse targets at a long-distance of 2 km in an outdoor environment. We also verified coherent LiDAR on a fiber array using OPAs for beam steering, employed FMCW LiDAR with triangular frequency-wave modulation and achieved simultaneous distance and velocity measurements. Furthermore, demonstrated 8 Gbps data transmission over a 3 km distance with a fiber-based OPA. The advantages of this design include a fast-steering speed, high power, and array

scalability. Future work will involve scaling to more array elements and reducing the array spacing, which may lead to a greater sidelobe suppression and higher lobe intensity.

Funding

Laser ranging detector. (E12701SZCZ).

CRediT authorship contribution statement

Yunhan Wu: Conceptualization, Methodology, Investigation, Writing – original draft, Writing – review & editing. **Shuai Shao:** Funding acquisition, Supervision, Project administration. **Yixuan Li:** Software, Formal analysis. **Xiangzheng Chen:** . **Dongbo Che:** Resources, Formal analysis. **Jiayu Chen:** Data curation. **Kunyang Du:** Resources. **Ruitao Jiang:** Resources. **Xunqing Huang:** Resources. **Dongping Kan:** .

Declaration of Competing Interest

The authors declare that they have no known competing financial interests or personal relationships that could have appeared to influence the work reported in this paper.

References

[1] T. Xia, M. Yang, R. Yang, Vision based global localization for intelligent vehicles, in: 2006 IEEE Intelligent Vehicles Symposium, IEEE, 2006, pp. 571–576.
[2] J.-F. Lalonde, N. Vandapel, D.F. Huber, M. Hebert, Natural terrain classification using three-dimensional ladar data for ground robot mobility, Journal of field robotics 23 (10) (2006) 839–861.
[3] J.H. Schween, A. Hirsikko, U. Löhnert, S. Crewell, Mixing-layer height retrieval with ceilometer and doppler lidar: from case studies to longterm assessment, Atmospheric, Measurement Techniques 7 (11) (2014) 3685–3704.
[4] M.A. Lefsky, W.B. Cohen, G.G. Parker, D.J. Harding, Lidar remote sensing for ecosystem studies: Lidar, an emerging remote sensing technology that directly measures the three-dimensional distribution of plant canopies, can accurately estimate vegetation structural attributes and should be of particular interest to forest, landscape, and global ecologists, BioScience 52 (2002) 19–30.
[5] C. Errando-Herranz, N. Le Thomas, K.B. Gylfason, Low-power optical beam steering by microelectromechanical waveguide gratings, Optics Letters 44 (4) (2019) 855, https://doi.org/10.1364/OL.44.000855.
[6] Y. Wang, G. Zhou, X. Zhang, K. Yu, M. C. Wu, 160× 160 mems-based 2-d optical phased array, in: CLEO: Science and Innovations, Optical Society of America, 2018, pp. SM3I–3.
[7] F. Xiao, L. Kong, Optical multi-beam forming method based on a liquid crystal optical phased array, Applied Optics 56 (36) (2017) 9854, https://doi.org/10.1364/AO.56.009854.
[8] D.N. Hutchison, J. Sun, J.K. Doylend, R. Kumar, J. Heck, W. Kim, C.T. Phare, A. Feshali, H. Rong, High-resolution aliasing-free optical beam steering, Optica 3 (8) (2016) 887, https://doi.org/10.1364/OPTICA.3.00088710.1364/OPTICA.3.000887.s001.
[9] S.(. Yin, J.H. Kim, F. Wu, P. Ruffin, C.(. Luo, Ultra-fast speed, low grating lobe optical beam steering using unequally spaced phased array technique, Optics communications 270 270 (1) (2007) 41–46.
[10] J. Sun, E. Timurdogan, A. Yaacobi, Z. Su, E.S. Hosseini, D.B. Cole, M.R. Watts, Large-scale silicon photonic circuits for optical phased arrays, IEEE journal of selected topics in quantum electronics 20 (2013) 264–278.
[11] C.V. Poulton, M.J. Byrd, P. Russo, E. Timurdogan, M. Khandaker, D. Vermeulen, M. R. Watts, Long-range lidar and free-space data communication with high-performance optical phased arrays, IEEE Journal of Selected Topics in Quantum Electronics 25 (5) (2019) 1–8.
[12] E. Timurdogan, Z. Su, C. V. Poulton, M. J. Byrd, S. Xin, R.-J. Shiue, B. R. Moss, E. S. Hosseini, M. R. Watts, Aim process design kit (aimpdkv2. 0): Silicon photonics passive and active component libraries on a 300mm wafer, in: Optical Fiber Communication Conference, Optical Society of America, 2018, pp. M3F–1.
[13] H. Abediasl, H. Hashemi, Monolithic optical phased-array transceiver in a standard soi cmos process, Optics express 23 (5) (2015) 6509, https://doi.org/10.1364/OE.23.006509.
[14] SungWon Chung, H. Abediasl, H. Hashemi, A monolithically integrated largescale optical phased array in silicon-on-insulator cmos, IEEE Journal of Solid-State Circuits 53 (1) (2018) 275–296.
[15] J.C. Hulme, J.K. Doylend, M.J.R. Heck, J.D. Peters, M.L. Davenport, J. T. Bovington, L.A. Coldren, J.E. Bowers, Fully integrated hybrid silicon two dimensional beam scanner, Optics express 23 (5) (2015) 5861, https://doi.org/10.1364/OE.23.005861.
[16] X. Cao, G. Qiu, K. Wu, C. Li, J. Chen, Lidar system based on lens assisted integrated beam steering, Optics Letters 45 (20) (2020) 5816, https://doi.org/10.1364/OL.401486.
[17] C. Li, X. Cao, K. Wu, X. Li, J. Chen, Lens-based integrated 2d beamsteering device with defocusing approach and broadband pulse operation for lidar application, Optics express 27 (23) (2019) 32970, https://doi.org/10.1364/OE.27.032970.
[18] P.F. McManamon, P.J. Bos, M.J. Escuti, J. Heikenfeld, S. Serati, H. Xie, E. A. Watson, A review of phased array steering for narrow-band electrooptical systems, Proceedings of the IEEE 97 (6) (2009) 1078–1096.
[19] W.R. Huang, J. Montoya, J.E. Kansky, S.M. Redmond, G.W. Turner, A. Sanchez-Rubio, High speed, high power one-dimensional beam steering from a 6-element optical phased array, Optics express 20 (16) (2012) 17311, https://doi.org/10.1364/OE.20.017311.
[20] C. Mekhiel, X. Fernando, Monolithic silicon-on-insulator optical beam steering with phase locking heterodyne feedback[C]//2017 IEEE 28th Annual International Symposium on Personal, Indoor, and Mobile Radio Communications (PIMRC), IEEE (2017) 1–5.
[21] C. V. Poulton, D. Vermeulen, E. Hosseini, E. Timurdogan, Z. Su, B. Moss, M. R. Watts, Lens-free chip-to-chip free-space laser communication link with a silicon photonics optical phased array, in: Frontiers in Optics, Optical Society of America, 2017, pp. FW5A–3.
[22] B. Guan, R.P. Scott, C. Qin, N.K. Fontaine, T. Su, C. Ferrari, M. Cappuzzo, F. Klemens, B. Keller, M. Earnshaw, S.J.B. Yoo, Free-space coherent optical communication with orbital angular, momentum multiplexing/demultiplexing using a hybrid 3d photonic integrated circuit, Optics express 22 (1) (2014) 145, https://doi.org/10.1364/OE.22.000145.
[23] H.-W. Rhee, J.-B. You, H. Yoon, K. Han, M. Kim, B.G. Lee, S.-C. Kim, H.-H. Park, 32 gbps data transmission with 2d beam-steering using a silicon optical phased array, IEEE Photonics Technology Letters 32 (13) (2020) 803–806.
[24] M. Raval, A. Yaacobi, M.R. Watts, Integrated visible light phased array system for autostereoscopic image projection, Optics Letters 43 (15) (2018) 3678, https://doi.org/10.1364/OL.43.003678.
[25] F. Aflatouni, B. Abiri, A. Rekhi, A. Hajimiri, Nanophotonic projection system, Optics express 23 (16) (2015) 21012, https://doi.org/10.1364/OE.23.021012.
[26] C.V. Poulton, A. Yaacobi, D.B. Cole, M.J. Byrd, M. Raval, D. Vermeulen, M. R. Watts, Coherent solid-state lidar with silicon photonic optical phased arrays, Optics letters 42 (20) (2017) 4091, https://doi.org/10.1364/OL.42.004091.
[27] K.e. Wang, A. Nirmalathas, C. Lim, E. Wong, K. Alameh, H. Li, E. Skafidas, High-speed indoor optical wireless communication system employing a silicon integrated photonic circuit, Optics letters 43 (13) (2018) 3132, https://doi.org/10.1364/OL.43.003132.